Electronic Supplementary Material (ESI) for Journal of Materials Chemistry C.

Supplementary material

$Pb(Fe_{0.5}Nb_{0.5})O_3$–$BiFeO_3$-based multicalorics with room-temperature ferroic anomalies

Uroš Prah,[a,b,*] Magdalena Wencka,[c] Tadej Rojac,[a,b] Andreja Benčan[a,b] and Hana Uršič[a,b]

[a] Jožef Stefan Institute, Jamova cesta 39, 1000 Ljubljana, Slovenia.
[b] Jožef Stefan International Postgraduate School, Jamova cesta 39, 1000 Ljubljana, Slovenia.
[c] Institute of Molecular Physics, Polish Academy of Sciences, ul. Smoluchowskiego 17, 61-179 Poznań, Poland.
[*] Corresponding author: uros.prah@ijs.si

A. Sintering behavior of PFN–20BFO-based compositions

The optimal sintering temperatures were selected and verified by performing two dynamic sintering curve experiments. The measurements were recorded during heating using an optical dilatometer (Leitz Version 1A, Leitz, Wetzlar, Germany), where in all cases heating rate of 2 °C·min^{-1} was used. In the first step, dynamic sintering curve measurement was performed by heating the sample to its melting point (i.e., up to ~1200 °C), representing a reference for the total shrinkage and densification level of each composition (solid lines in Fig. S1). Based on that, the temperature at which the powder compact start to densify was selected. The temperature 900 °C was selected for pure and Mn-doped samples, while for Gd,Mn co-doped sample 1000 °C is required to obtain a sufficient degree of densification. In the next step, the dynamic sintering curve measurements were repeated by creating the entire sintering process, namely heating the powder compact to previously selected temperature followed by 2 hours of holding time at this temperature (open symbols in Fig. S1). In all three compositions, the selected thermal processes have led to sufficient densification of the powder compacts.

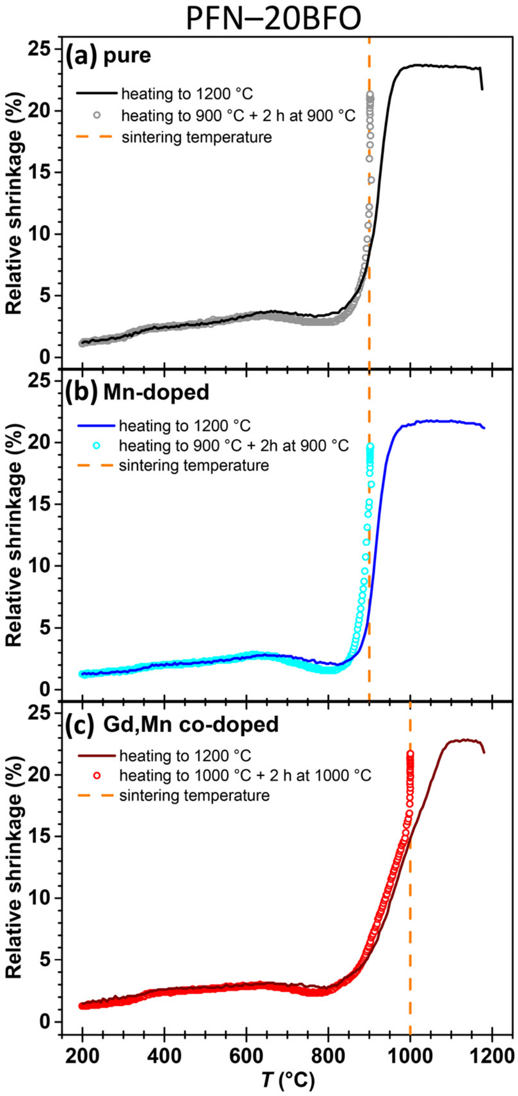

Fig. S1. Dynamic sintering curves measurements of (a) pure, (b) Mn-doped and (c) Gd,Mn co-doped PFN–20BFO powder compacts. Solid lines and open symbols represent shrinkage during heating to 1200 °C and during thermal treatment at selected sintering conditions, respectively.

B. Rietveld refinement of PFN–20BFO-based compositions

The quantitative phase composition analyses were performed using the Rietveld refinement method. For this purpose, the XRD patterns were recorded in the 15–120° 2θ-range with a step of 0.008° and an integration time of 100 s per step at RT. The *Topas R* package (version 2.1, Bruker, AXS, Karlsruhe, Germany) was employed and a Fundamental Parameters Approach was used to describe the peak profile.[a] In this model, the background (10th order Chebychev), unit cell parameters, crystallite size, scale factors, sample displacement, atomic coordinates, and thermal parameters were stepwise refined to obtain a calculated diffraction profile that best fits the experimental pattern. The quality of the fit was assessed from the goodness-of-fit parameters R_{wp}, R_{p}, R_{exp}, R_{B}, and *G.O.F.*

The effects of Mn and Gd doping on the phase composition, crystal structure and lattice parameters of PFN–20BFO were investigated. The agreement factors of the Rietveld analysis along with the cell parameters of all PFN–20BFO-based compositions are given in Table S1.

Table S1: Refined structural parameters for PFN–20BFO-based compositions at RT.

PFN–20BFO	**Pure**	**Mn-doped**	**Gd,Mn co-doped**
Crystal system	Cubic	Cubic	Cubic
Space group	$Pm\bar{3}m$	$Pm\bar{3}m$	$Pm\bar{3}m$
a (Å)	4.01038(9)	4.00917(5)	4.00441(1)
V (Å^3)	64.4999(9)	64.4414(3)	64.2119(1)
ρ (g·cm^{-3})	8.4123(5)	8.4062(6)	8.4042(2)
R_{wp} (%)	7.70	7.39	7.07
R_{exp} (%)	4.93	6.30	6.47
R_p (%)	5.89	5.69	5.49
G.O.F.	1.56	1.17	1.09
R_B (%)	2.46	3.19	4.39

The results of Rietveld refinement show that the addition of Mn as well as further doping with Gd ions does not affect the crystal symmetry at RT, which in all three PFN–20BFO-based compositions remains pseudocubic with $Pm\bar{3}m$ space group (Fig. S2a). Furthermore, doping with Mn ions leads to a slight decrease of the lattice parameter and unit cell volume (Fig. S2b). This could be consequence of a smaller ionic radius of Mn^{4+} (53 pm) compared to Fe^{3+} (64.5 pm for high spin configurations) and Nb^{5+} (64 pm) on B-site of the perovskite structure.[b] The decrease is even more pronounced in Gd,Mn co-doped sample, where additional contraction of lattice constants most probably arise from smaller ionic radius of Gd^{3+} (93.8 pm) compared to Bi^{3+} (103 pm) on A-site of the perovskite structure.[b]

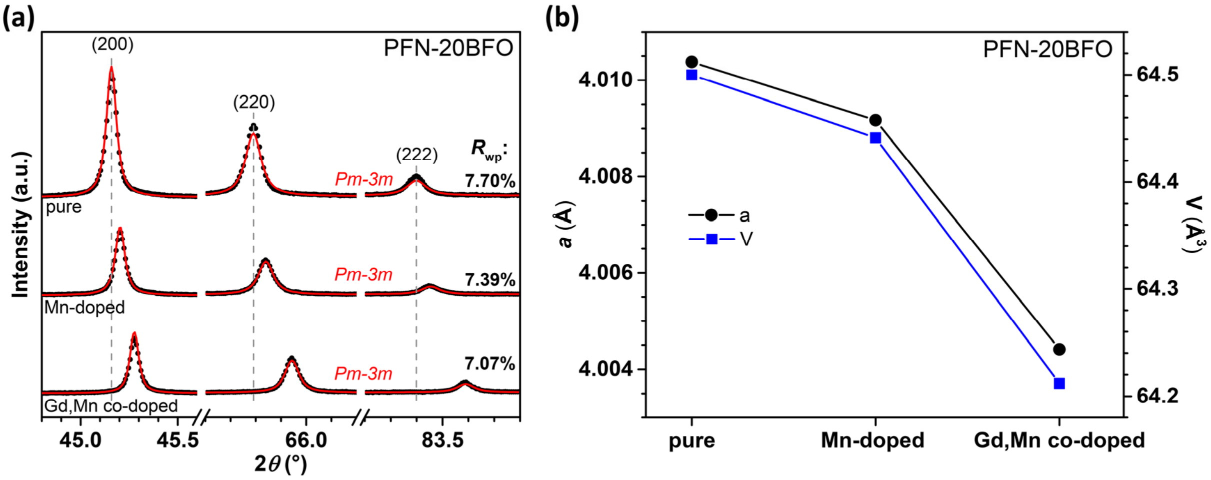

Fig. S2. (a) Room-temperature XRD profiles of the *200*, *220*, and *222* pseudocubic reflections (only from Cu $K\alpha_1$) for PFN–20BFO-based compositions. The calculated profile for the pseudocubic phase ($Pm\bar{3}m$ space group) is displayed in red. (b) Lattice parameters and unit cell volumes of PFN–20BFO-based compositions. Lines between the measured values are just a guide to the eye.

C. Measurements of magnetic properties of PFN–BFO-based compositions

M–H hysteresis loops of PFN–100*x*BFO ($x = 0$–0.5) solid solutions measured at 25 °C and −270 °C at the magnetic field of 90 kOe are shown in Fig. S3. At RT, compositions with $x < 0.5$ exhibit linear, paramagnetic-like *M–H* response (Fig. S3a), while in PFN–50BFO a weak antiferromagnetic behavior is present (inset of Fig. S3a). This is consistent with the results of *M*(*T*) measurements (Fig. 2 in the main text), which reveal that PFN–50BFO exhibits paramagnetic-antiferromagnetic phase transition above RT. At −270 °C, the presence of antiferromagnetic behavior is observed in all compositions (Fig. S3b). The coercive magnetic field (H_c), remanent magnetization (M_R) and saturated magnetization (M_S) are decreased with increasing amount of BFO, reaching the maximum values in PFN, namely ~1.8 kOe, ~0.1 emu·g^{-1} and ~2.2 emu·g^{-1}, respectively. This is in agreement with the *M*(*T*) measurements (Fig. 2 in the main text), where in PFN the highest *M* values are obtained. A reason for such behavior at low temperatures is the formation of a spin-glass-like phase in PFN-rich compositions, which arises from local short range order on the B-site perovskite sublattice (namely from Nb-rich-Fe-poor regions), where long range antiferromagnetic order is disturbed due to the presence of nonmagnetic Nb^{5+} ions. Therefore, an increase in Nb^{5+} concentration and thus Nb/Fe ratio increases the tendency for the formation of short-range spin-glass-like phase at low temperatures, which is reflected in higher *M* values in PFN-rich PFN–BFO compositions.[c,d,e]

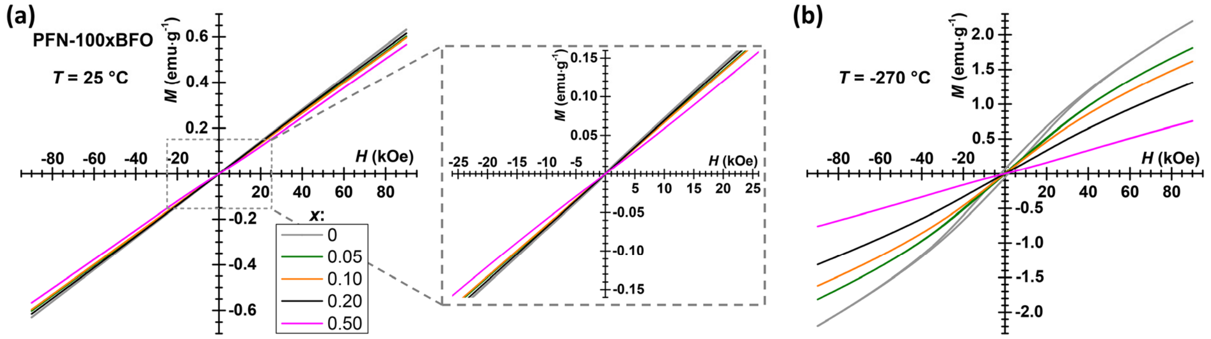

Fig. S3. *M–H* hysteresis loops of PFN–100*x*BFO ($x = 0$–0.5) measured at (a) 25 °C and (b) −270 °C. Inset: the enlarged view of the data between ±25 kOe at 25 °C.

The temperature dependences of *M* at different *H* for all three PFN–20BFO-based compositions are shown in Fig. S4. In all cases, *M* increases with decreasing temperature reaching maximum values at −270 °C. Such *M*(*T*,*H*) measurements were used for calculation of MC effect using indirect method.[f]

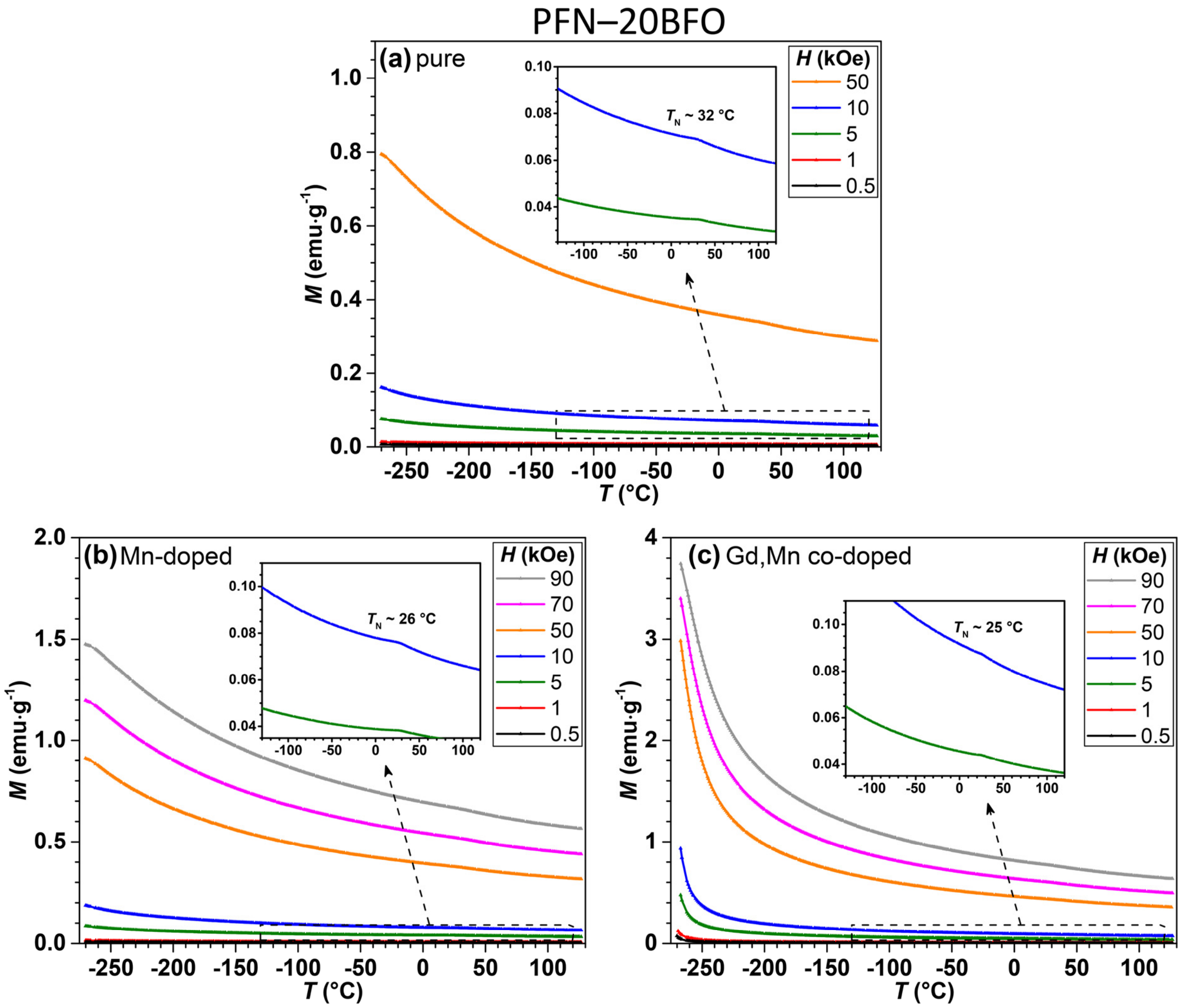

Fig. S4. Temperature dependences of M at different applied H for (a) pure, (b) Mn-doped and (c) Gd,Mn co-doped PFN–20BFO. Insets: the enlarged view of the data between −130 °C and 120 °C where T_{N} is highlighted.

D. Multicaloric properties of pure PFN–20BFO

First, the EC effect of PFN–20BFO solid solution was measured. The temperature dependence of ΔT_{EC} at different applied electric fields is shown in Fig. S5a. The ΔT_{EC} of 0.91 °C was obtained at RT and 90 $\mathrm{kV{\cdot}cm^{-1}}$ (determined directly from measured temperature change during the EC cycle, shown in Fig. S5b). At higher temperatures ΔT_{EC} slightly increases reaching a maximum value of 0.94 °C at 45 °C and 90 $\mathrm{kV{\cdot}cm^{-1}}$. Measurements at higher temperatures and larger applied electric fields were not possible due to the excessive electrical conductivity. Namely, the increased electrical conductivity leads to the appearance of Joule heating (JH) that can slightly or completely overlap the ΔT_{EC} (marked with crosses in Fig. S5a) and thus critically degrade the cooling ability of the material[g] (details in the next section, E). For example, the JH is 0.41 °C at RT and 90 $\mathrm{kV{\cdot}cm^{-1}}$ (Fig. S5b). Taking into account the influence of JH on total EC cooling effect, the term EC effective cooling (ΔT_{eff}), defined as a difference between ΔT_{EC} and ΔT_{JH}, was introduced (shown in Figs. S5b and S6). The temperature and electric field dependence of ΔT_{eff} is shown in Fig. S5c. The highest ΔT_{eff} value of 0.50 °C was obtained at RT and 90 kV·cm^{-1}. Due to increased JH, ΔT_{eff} is significantly reduced at higher temperatures, namely to only 0.17 °C at 45 °C and 90 kV·cm^{-1}.

The temperature dependences of ΔT_{MC} (calculated from $M(T)$ curves shown in the previous section, C) at different applied magnetic fields are shown in Fig. S5d. In general, ΔT_{MC} is low through the entire measuring temperature range reaching the maximum value of only 0.07 °C at −270 °C and 50 kOe. Additionally, at RT a peak in ΔT_{MC} response is observed (inset of Fig. S5d) in agreement with paramagnetic-antiferromagnetic phase transition. The peak value of ΔT_{MC} is ~$1.5\cdot10^{-3}$ °C at 42 °C and 50 kOe, which is comparable to the room-temperature value of PFN ceramics.[g]

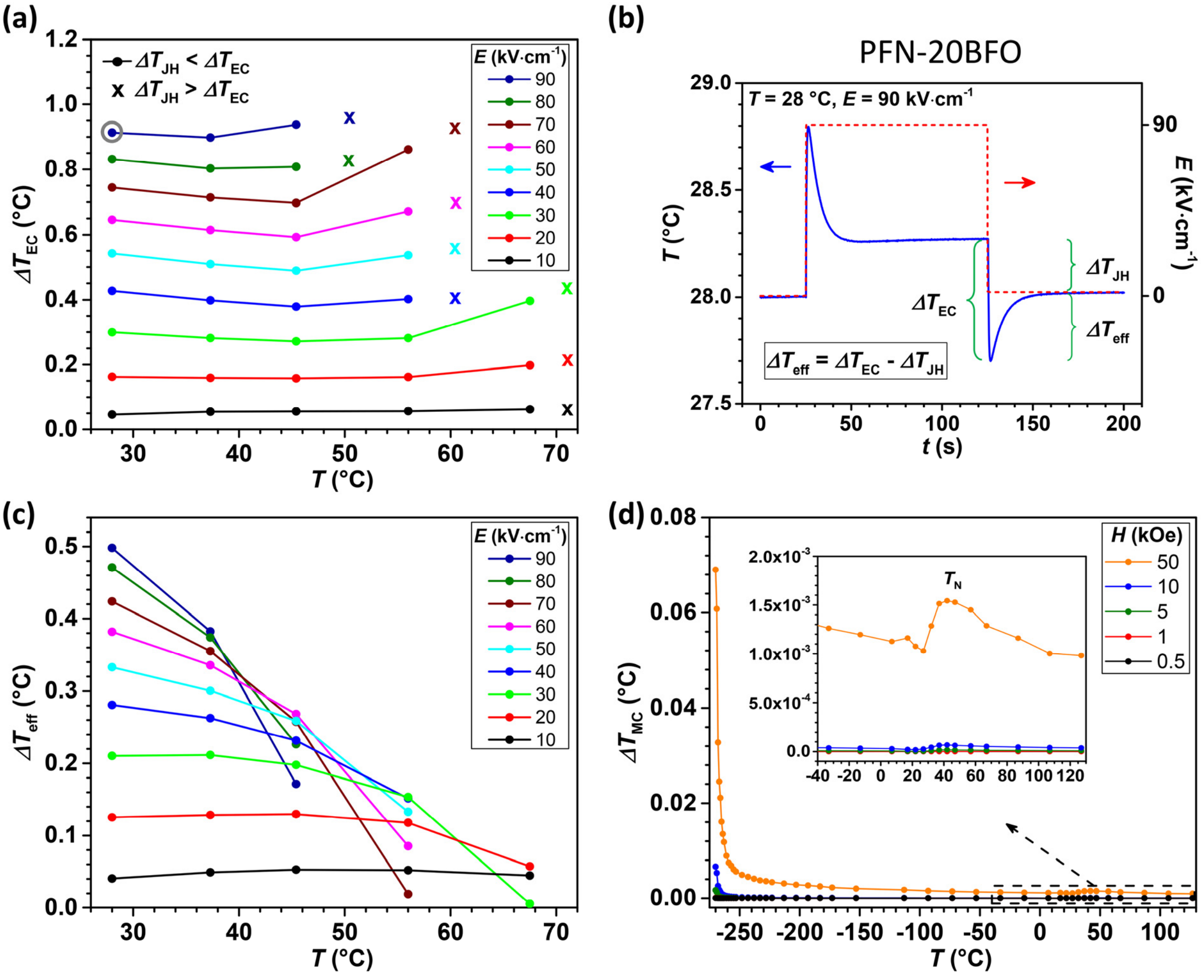

Figure S5. Multicaloric properties of PFN–20BFO; (a) ΔT_{EC} with (b) corresponding measured temperature change during the EC cycle at 28 °C and 90 kV·cm^{-1} (marked with gray circle in panel a) and (c) ΔT_{eff} measured at different temperatures and applied electric fields. The crosses in (a) mark the measurements where ΔT_{JH} overlap ΔT_{EC}. Note that temperature changes in (b) are not multiplied by a correction factor of 1.6. (d) ΔT_{MC} measured at different temperatures and applied magnetic fields with the inset showing an enlarged view of the data between −40 °C and 130 °C. Lines between the measured values are just a guide to the eye.

E. Electrocaloric effective cooling

Two examples of the measured temperature changes during the EC cycle in PFN–20BFO-based compositions are shown in Fig. S6. To determine the influence of Joule heating on the overall EC cooling response, the term EC effective cooling (ΔT_{eff}), defined as a difference between the EC temperature change (ΔT_{EC}) and temperature change corresponding to the Joule heating (ΔT_{JH}), was introduced. In the first example, i.e., the temperature change during the EC cycle of Gd,Mn co-doped sample at 56 °C and 100 kV·cm^{-1}, no Joule heating is present, therefore ΔT_{eff} is identical to ΔT_{EC} (Fig. S6a). While, in the second example, i.e., the temperature change during the EC cycle of pure PFN–20BFO at 28 °C and 50 kV·cm^{-1}, ΔT_{eff} is lower in comparison to ΔT_{EC}, due to the appearance of Joule heating effect (Fig. S6b).

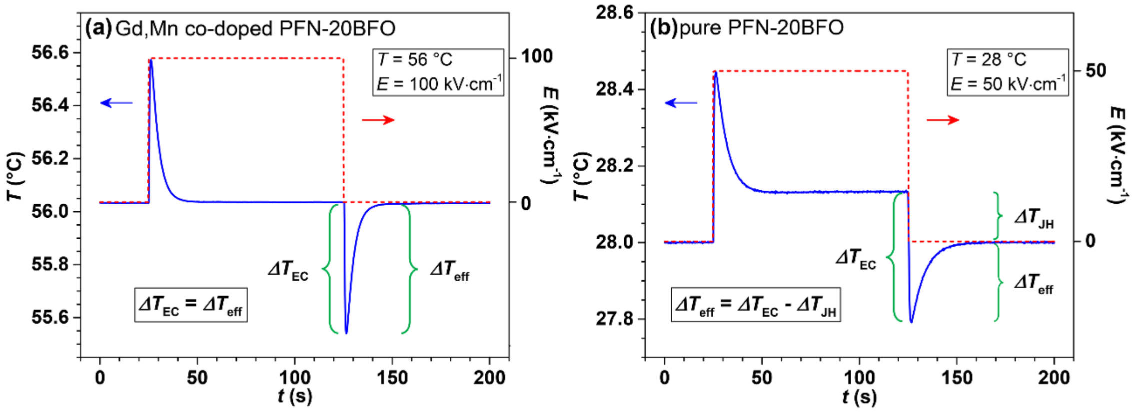

Fig. S6. Measured temperature changes during the EC cycle. The measurements were obtained (a) in Gd,Mn co-doped PFN–20BFO at 56 °C and 100 kV·cm^{-1} and (b) in pure PFN–20BFO at 28 °C and 50 kV·cm^{-1}. The applied electric field signal is marked by red dotted line. Note that temperature changes in (a) and (b) are not multiplied by a correction factor of 1.6 and 1.7, respectively.

F. EDXS analysis of Gd,Mn co-doped PFN–20BFO

Identification of the secondary phases present in Gd,Mn co-doped PFN–20BFO sample was performed by SEM-EDXS point analysis using accelerating voltage of 15 kV. SEM image of polished surface reveals the presence of two different secondary phases, which are marked with red and blue arrows in Fig. S7a. The EDXS analyses of identified secondary phases together with the matrix phase are shown in Fig. S7b. EDXS analysis reveal that areas marked with red arrows correspond to Fe-rich secondary phase, while areas marked with blue arrows indicating the presence of Gd,Nb-rich secondary phase. Considering the standard deviation error, the composition of a matrix phase is very close to the nominal value. Note that due to the small size of both secondary phases in comparison to ~1 μm large interaction volume of EDXS analysis, the results are only used for qualitative comparison. In addition, the amount of Mn is below the detection limit of the technique.

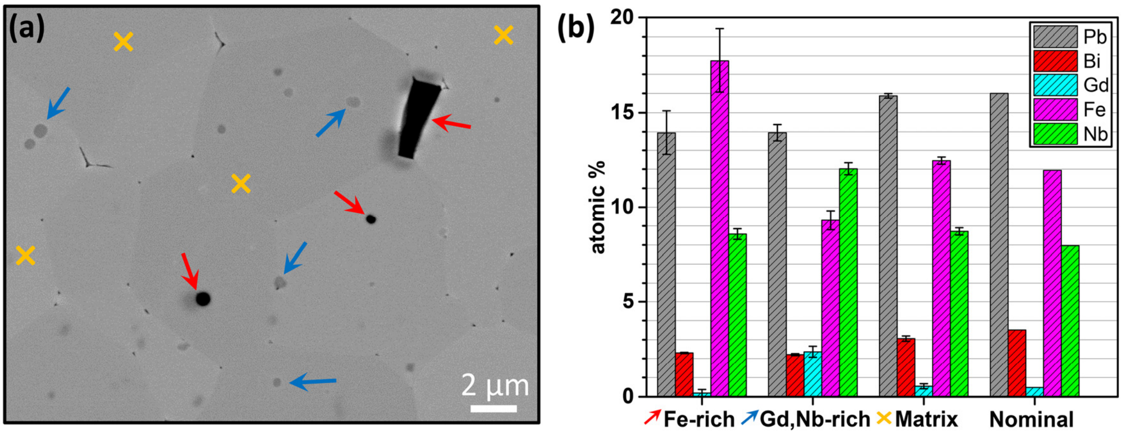

Fig. S7. (a) SEM micrograph of polished Gd,Mn co-doped PFN–20BFO with red arrows, blue arrows and orange crosses indicating Fe-rich, Gd,Nb-rich secondary phases and the matrix phase, respectively. (b) Corresponding EDXS analysis of phases marked with red arrows, blue arrows, orange crosses and nominal composition, respectively. Results are presented as average values with standard deviations of at least three areas.

G. Microstructure and grain size distributions of PFN–20BFO-based compositions

SEM images of the fractured, thermally etched surfaces and grain size distributions of all three PFN–20BFO-based compositions are shown in Fig. S8. In all compositions, SEM images reveal uniform and dense microstructures. Furthermore, in the thermally etched image of pure PFN–20BFO also some pull-outs, produced during the sample surface preparation, are present, while in Gd,Mn co-doped sample traces of Fe- and Gd,Nb-rich secondary phases are visible as a dark phase regions (described in the previous section, F). In all samples, a unimodal grain size distribution is observed (Fig. S8c).

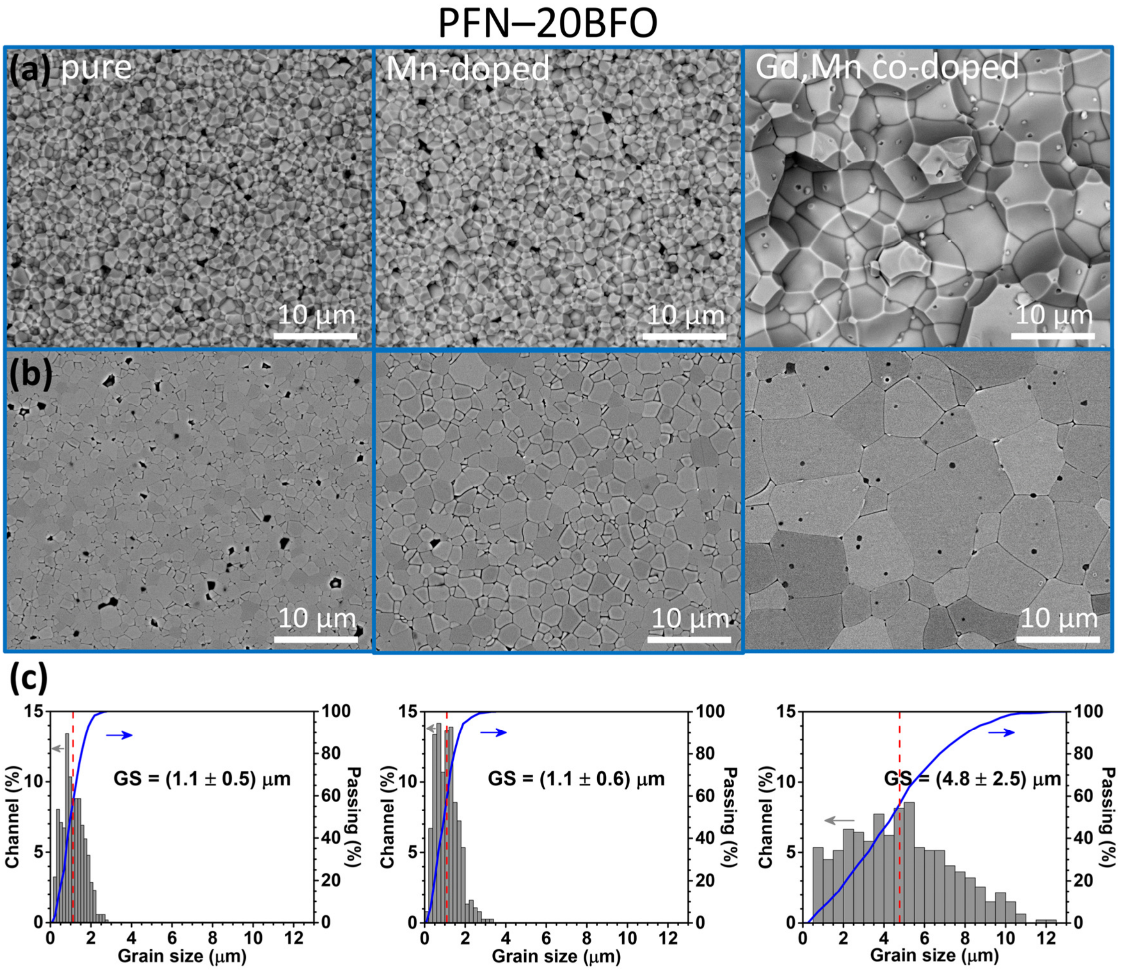

Fig. S8. SEM images of (a) fractured, (b) thermally etched surfaces and (c) the grain size distributions of PFN–20BFO-based compositions.

References

[a] R. W. Cheary and A. Coelho, *J. Appl. Crystallogr.*, 1992, **25**, 109–121.

[b] R. D. Shannon, *Acta Cryst. A*, 1976, **32**, 751–767.

[c] A. Kumar, R. S. Katiyar, C. Rinaldi, S. G. Lushnikov and T. A. Shaplygina, *Appl. Phys. Lett.*, 2008, **93**, 232902 1–3.

[d] G. M. Rotaru, B. Roessli, A. Amato, S. N. Gvasaliya, C. Mudry, S. G. Lushnikov and T. A. Shaplygina, *Phys. Rev. B*, 2009, **79**, 184430 1–5.

[e] V. V. Laguta, J. Rosa, L. Jastrabik, R. Blinc, P. Cevc, B. Zalar, M. Remskar, S. I, Raevskaya and I. P. Raevski, *Mater. Res. Bull.*, 2010, **45**, 1720–1727.

[f] A. M. Tishin and Y. I. Spichkin. The Magnetocaloric Effect and its Applications, Institute of Physics Publishing, Bristol, UK, (2003).

[g] A. Bradesko, A. Hedl, L. Fulanovic, N. Novak and T. Rojac, *APL Mater.*, 2019, **7**, 071111 1–6.

[h] U. Prah, T. Rojac, M. Wencka, M. Dragomir, A. Bradesko, A. Bencan, R. Sherbondy, G. Brennecka, Z. Kutnjak, B. Malic and H. Ursic, *J. Eur. Ceram. Soc.*, 2019, **39**, 4122–4130.